A&A 541, A68 (2012)
DOI: 10.1051/0004-6361/201218866

Astronomy & Astrophysics

Vortices, shocks, and heating in the solar photosphere: effect of a magnetic field

R. Moll, R. H. Cameron, and M. Schüssler

Max-Planck-Institut für Sonnensystemforschung, Max-Planck-Straße 2, 37191 Katlenburg-Lindau, Germany
e-mail: `msch@mps.mpg.de`

Received 23 January 2012 / Accepted 21 March 2012

ABSTRACT

Aims. We study the differences between non-magnetic and magnetic regions in the flow and thermal structure of the upper solar photosphere.

Methods. Radiative MHD simulations representing a quiet region and a plage region, respectively, which extend into the layers around the temperature minimum, are analyzed.

Results. The flow structure in the upper photospheric layers of the two simulations is considerably different: the non-magnetic simulation is dominated by a pattern of moving shock fronts while the magnetic simulation shows vertically extended vortices associated with magnetic flux concentrations. Both kinds of structures induce substantial local heating. The resulting average temperature profiles are characterized by a steep rise above the temperature minimum due to shock heating in the non-magnetic case and by a flat photospheric temperature gradient mainly caused by Ohmic dissipation in the magnetic run.

Conclusions. Shocks in the quiet Sun and vortices in the strongly magnetized regions represent the dominant flow structures in the layers around the temperature minimum. They are closely connected with dissipation processes providing localized heating.

Key words. Sun: photosphere – Sun: chromosphere – magnetohydrodynamics (MHD) – convection – Sun: surface magnetism

1. Introduction

Semi-empirical models of strongly magnetized regions in the solar atmosphere (such as network and plage areas) indicate increased temperatures relative to the "quiet" Sun (e.g. Fontenla et al. 2006). This is consistent with the fact that individual magnetic structures are hotter than their surroundings in the upper layers of the photosphere and in the chromosphere (e.g. Solanki 1993; Lagg et al. 2010), but the nature of the concomitant heating process is still under debate. One possibility is the dissipation of mechanical energy in the form of flows or waves, another is resistive dissipation of magnetic energy, for instance in current sheets.

The dynamics in these atmospheric layers is complex and diverse. For the weakly magnetized internetwork regions, numerical simulations and observations (e.g. Carlsson & Stein 1992, 1997; Wedemeyer et al. 2004; Wedemeyer-Böhm 2010) suggest that shocks driven by overshooting convection play an important part above the temperature-minimum region. In addition, swirling motions have been detected in observations of the chromosphere (Wedemeyer-Böhm & Rouppe van der Voort 2009), the transition region (Curdt et al. 2012), and the corona (Zhang & Liu 2011).

Small-scale vortices occuring in simulations of non-magnetic or weakly magnetized regions of the lower atmosphere and uppermost convection zone were studied by Moll et al. (2011) and Kitiashvili et al. (2011). Simulations comprising sufficient magnetic flux to represent network patches or plage regions exhibit vertically orientated vortices associated with magnetic flux concentrations in the upper photosphere and lower chromosphere (Vögler 2004; Shelyag et al. 2011; Carlsson et al. 2010; Kitiashvili et al. 2012; Steiner & Rezaei 2012).

In this paper, we analyze simulations extending higher into the lower chromosphere for a detailed study of the effect of a magnetic field on the flow structure as well as on the heating processes in the atmosphere up to a few hundred km above the average height of the temperature minimum. We compare a simulation without magnetic field as an extreme case of "quiet Sun" with a simulation having a mean vertical field of 200 G, which is considered to represent the conditions in a plage region.

2. Methods

2.1. Simulations

We analyzed simulations carried out with the `MURaM` code (for a detailed description, see Vögler 2003; Vögler et al. 2005), which treats the equations of compressible MHD together with the radiative transfer equation solved along 12 rays per grid cell. The equation of state incorporates the effect of partial ionization for 11 elements. The numerical scheme uses 4th-order centered spatial differences and a 4th-order Runge-Kutta method for the time stepping. Both the top and bottom boundaries permit free in- and outflow of fluid, the side boundaries are periodic. The magnetic field at the top and bottom boundaries is assumed to be vertical.

Here we consider two simulation runs, one non-magnetic and one with an average unipolar vertical magnetic field of 200 G. Both runs used a computational box with a horizontal area of $6 \times 6\,\mathrm{Mm}^2$ and a height of 1.68 Mm, ranging from about 900 km below the average height of the optical surface to roughly 800 km above. The size of the grid cells was $20.8 \times 20.8 \times 14.0\,\mathrm{km}^3$. The simulations were run for several hours solar time to reach a statistically stationary state. For the statistical analyses, we used 4 snapshots from each run.

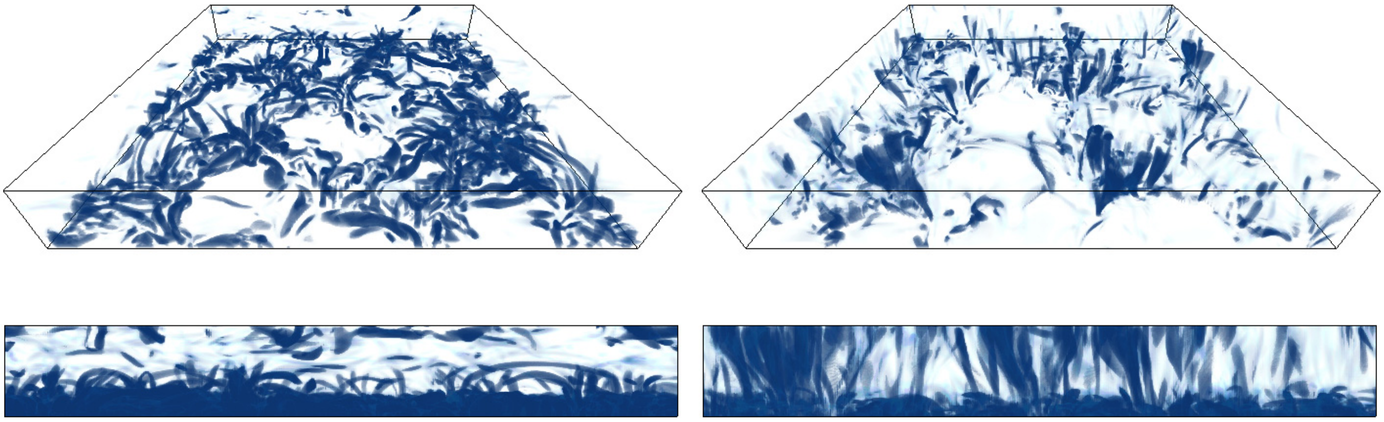

Fig. 1. Volume rendering of the swirling strength, $\lambda_{\rm ci}$, in the non-magnetic case (*left*) and the magnetic case (*right*) from two viewing angles. Shown is the upper half ($6 \times 6 \times 0.8\,{\rm Mm}^3$) of the computational domain, the bottom plane corresponding roughly to the optical surface. The color scale covers the range $0 \leq \lambda_{\rm ci} \leq 0.027\,{\rm s}^{-1}$; higher values of $\lambda_{\rm ci}$ are saturated.

2.2. Vortex identification

The vorticity is not the optimal quantity to identify swirling flows. For instance, a purely bidirectional shear flow without any rotational component nevertheless has a non-vanishing vorticity. For the detection of vortices, i.e., fluid elements rotating about a local, possibly moving axis, we followed the procedure employed in Moll et al. (2011): vortices (swirling flows) are defined as regions where the velocity gradient tensor has a pair of complex conjugate eigenvalues (Zhou et al. 1999). The strength of the vortical motion is determined by the *swirling strength*, $\lambda_{\rm ci}$, which is the magnitude of the unsigned imaginary part of the complex eigenvalues. In the case of rigid rotation, we have $\lambda_{\rm ci} = 2\pi/\tau_{\rm s}$, where $\tau_{\rm s}$ is the rotation (or swirling) period. The direction of a vortex is defined to be along the eigenvector corresponding to the real eigenvalue. The inclination angle of this vector with respect to the vertical direction is denoted with ι.

3. Results

3.1. Vortex properties

Figure 1 shows regions of high swirling strength in snapshots from the non-magnetic and magnetic simulations, respectively. The most striking difference between the two cases is the dominance of tall, vertically orientated vortices in the magnetic case, which extend over the entire height of the simulated photosphere. In the non-magnetic case, the vortex features do not protrude far above the optical surface, bending over to form mainly horizontally orientated loops. Vortex features near the top of the computational domain are associated with shock fronts (see Sect. 3.2). The difference between the two simulations is further illustrated in Fig. 2, which shows the location of vertical ($\iota < 20°$, left column) and horizontal ($\iota > 70°$, right column) vortices on horizontal planes. In the upper two rows, the vortex locations are compared to the distribution of vertical velocity at the average height of the optical surface ($z = 0$). Near the optical surface, both simulations show horizontal vortices at the edges of granules and vertical vortices in the intergranular downflows lanes. The comparison with the magnetic-field distribution in the third row indicates that the horizontal vortices near $z = 0$ are a hydrodynamical phenomenon of the overturning motions at the borders of granules, which is essentially unrelated to the intergranular magnetic flux concentrations (cf. Steiner et al. 2010; Moll et al. 2011). In contrast to this, the vertical vortices are almost exclusively found in magnetic flux concentrations. This one-to-one relationship extends throughout the atmosphere, as shown in the bottom row of Fig. 2, which corresponds to a height of $z = 644$ km above the average optical surface. At this height, we find a multitude of vertical vortices in the (expanded) flux concentrations, while strong horizontal vortices are absent.

The visual impression provided by Figs. 1 and 2 is confirmed quantitatively in Fig. 3, which shows height profiles of horizontally averaged vorticity, swirling strength, and the shear part of vorticity, $\omega_{\rm sh} = \omega - 2\lambda_{\rm ci}$, where ω is the modulus of the vorticity vector[1]. In the magnetic simulation, all three quantities are suppressed in the deeper layers up to $z \simeq 200$ km, owing to the effect of the Lorentz force on the convective motions. In the upper layers, the situation is reversed and the swirling and shearing motions are enhanced in comparison to the non-magnetic case. We surmise that this is caused by the dynamical coupling of the vortex motion in the convective near-surface layers to the upper layers, which is mediated by the mainly vertical magnetic field.

The drastic change in the properties of the vortex flows above about 150 km height is analyzed in more detail in Fig. 4, which shows height profiles of the fractions of horizontal area covered by swirls of different strength and orientation. In the non-magnetic case (upper panel), horizontal vortices dominate at all heights, but the area fraction of strong vortices (swirling period $\tau_{\rm s} < 2$ min) drops drastically above the optical surface. For the vertical vortices, the decrease starts even below the optical surface. The increase of horizontal vortices above about 500 km is probably related to the pattern of shock waves developing in these layers (see Sect. 3.2). In the magnetic case (lower panel of Fig. 4), the horizontal vortices behave very similar to those in the non-magnetic simulation, their area coverage dropping even faster with height. However, the area fraction of vertical vortices shows almost no drop above $z = 0$, followed by a strong increase above 200 km, from which height on they dominate. Virtually all swirls at large heights have vertical orientation ($\iota \lesssim 20°$) in the magnetic case. Even very strong vertical vortices with

---

[1] For a purely rotational flow, we have $\omega = 2\lambda_{\rm ci} = \omega_{\rm R}$ at the center of the vortex. Therefore, one can formally split the vorticity into a rotational part, $\omega_{\rm R}$, and the remainder, $\omega_{\rm sh} = \omega - \omega_{\rm R}$, which gives the contribution from locally non-rotating shear flow.

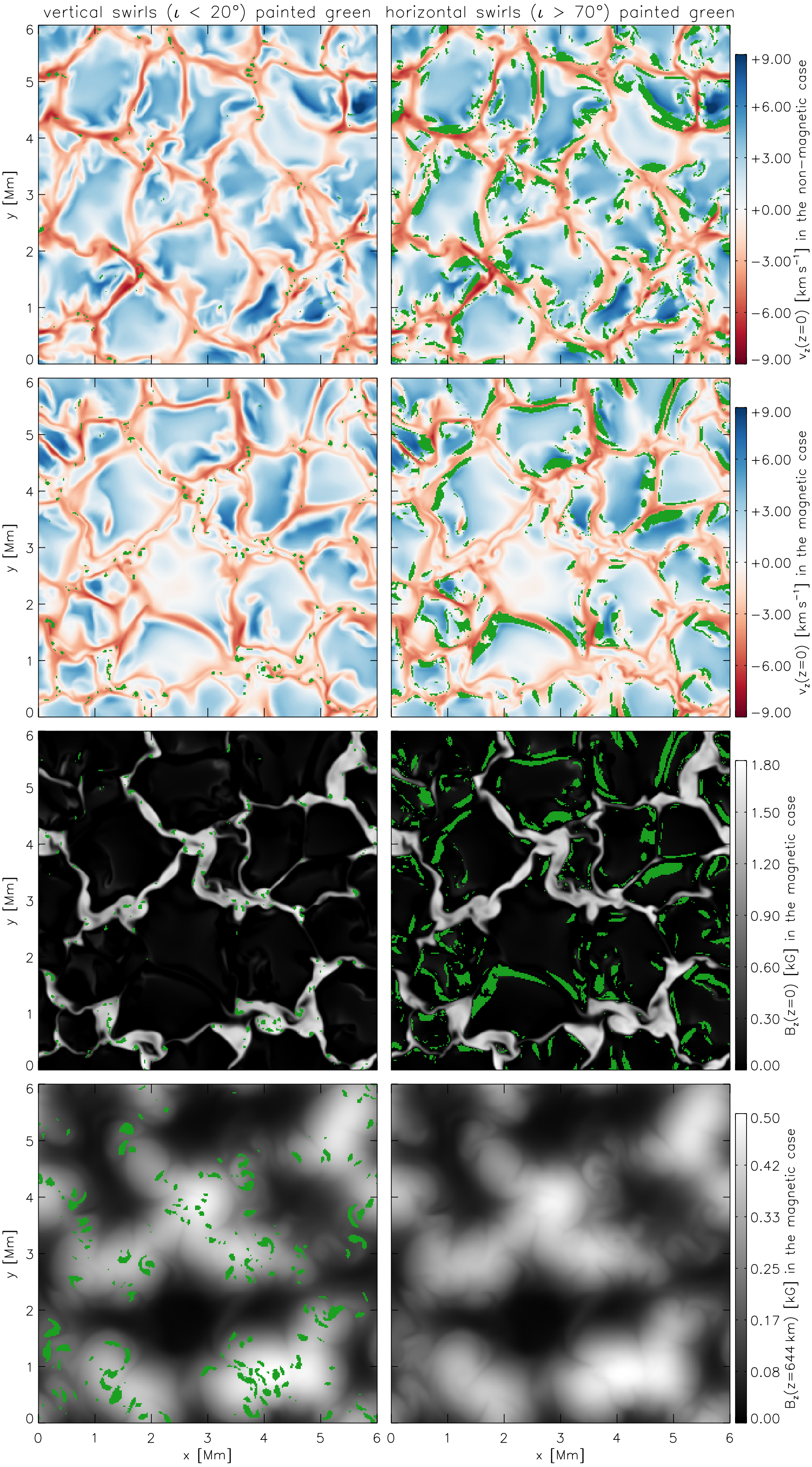

Fig. 2. Distribution of vertical vortices (inclination $\iota < 20°$, *left column*) and horizontal vortices ($\iota > 70°$, *right column*) on horizontal planes. Pixels corresponding to swirling periods $\tau_s < 240$ s are indicated in green color on cuts of the vertical velocity at $z = 0$ (average height of the optical surface) for the non-magnetic case (*top* row) and for the magnetic case (*second* row). Similarly, the strong swirls are indicated on maps of the vertical magnetic field component at $z = 0$ (*third* row) and at $z = 644$ km (*bottom* row) for the simulation with magnetic field.

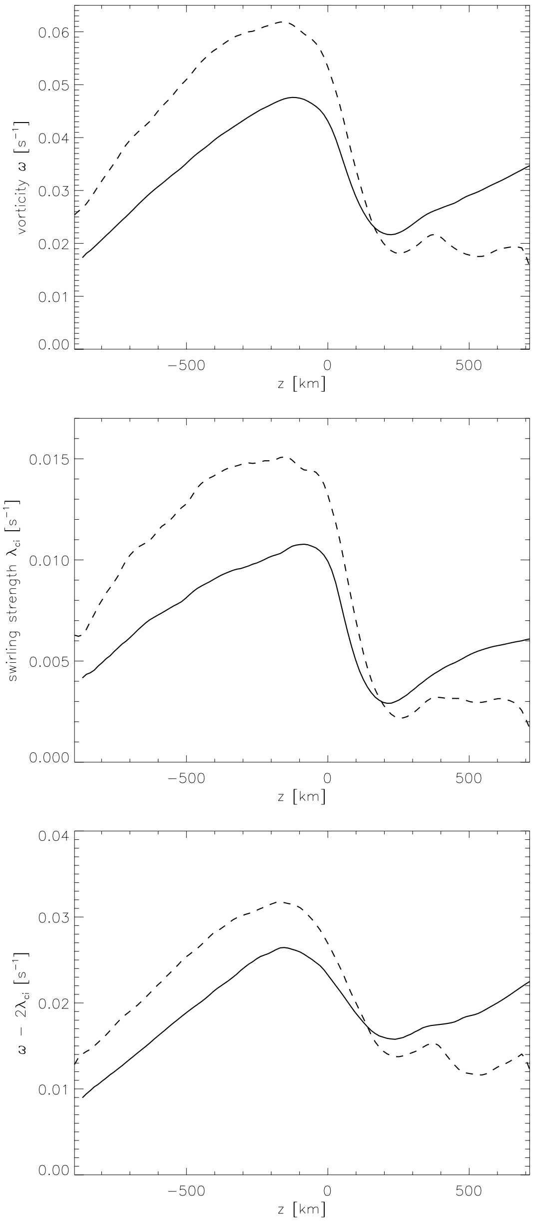

Fig. 3. Horizontal averages of vorticity (*top*), swirling strength (*middle*), and shear part of the vorticity (*bottom*), as functions of height. Solid lines correspond to the magnetic case, dashed lines to the non-magnetic case.

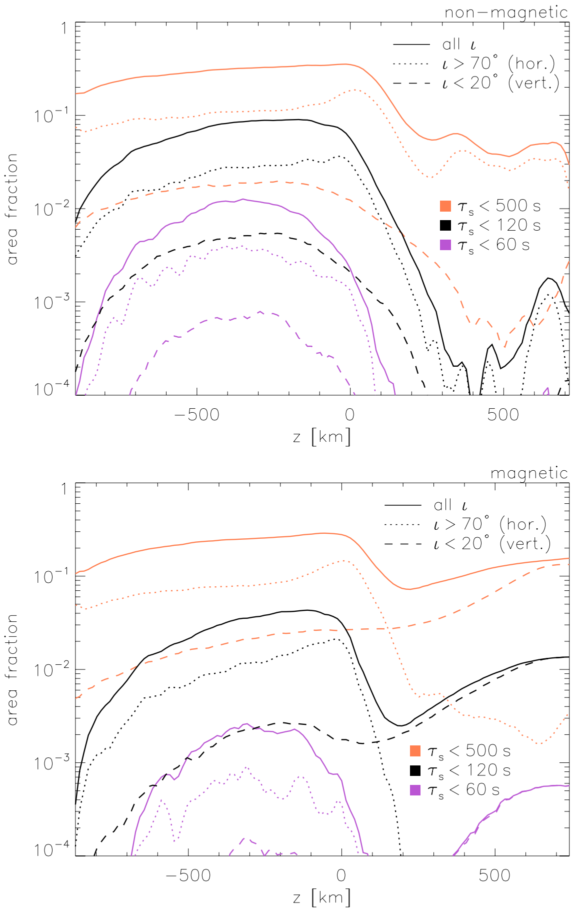

Fig. 4. Height profiles of the horizontal area fraction of grid cells with swirling period, $\tau_\mathrm{s} = 2\pi/\lambda_\mathrm{ci}$, below given thresholds in the non-magnetic case (*upper panel*) and in the magnetic case (*lower panel*). Full lines correspond to vortices of all inclinations, while dotted and dashed lines separately represent horizontal and vertical swirls, respectively.

periods below one minute reach appreciable area coverage above $z \simeq 400$ km.

Figure 5 shows histograms of vortex properties at three height ranges, one in the deep layers of the computational domain (brown curves), one straddling the optical surface (green curves), and one high in the photosphere (blue curves). While the vortices in the non-magnetic case (dashed curves) and the magnetic case (solid curves) do not strongly differ in the deep and the near-surface layers, they show strong deviations in the higher layer: in the magnetic run, the typical swirling periods are much smaller (i.e., the vortices are more vigorous) and the gas pressure is strongly reduced in comparison to the average gas pressure at the same height. The low pressure results from the location of the vortices in magnetic flux concentrations (cf. Fig. 2, bottom left panel), together with the effect of the centrifugal force. The temperatures of the weak swirls in the upper photosphere of the non-magnetic simulation are significantly higher than the average temperature, presumably due to their association with shock fronts. The vortices in the upper layers of the magnetic simulation are also hotter by 10–20% compared to their average surroundings. The vertical velocities in vortices do not differ strongly between the two simulations: in the deep and near-surface layers, vortices are predominantly located in downflows in both cases, while in the upper layer there is a slight preference for upflows in the non-magnetic case and an almost symmetric distribution around zero in the magnetic run.

3.2. Dynamics of the upper photosphere

High in the photosphere and above, the thermal and flow structure is very different in the two cases. Figures 6 and 7 show maps of various quantities on horizontal planes. In the non-magnetic case (Fig. 6), there is a pattern of shock fronts with regions of strongly localized heating, leading to a thermal bifurcation into hot and cool regions (cf. Wedemeyer et al. 2004). The generally inclined and propagating shock fronts form a rapidly evolving filamentary pattern on horizontal cuts of temperature and divergence of the horizontal velocity. Some of the shocks are associated with vortices, which are preferentially horizontally orientated (cf. Fig. 4, upper panel). An example of a shock

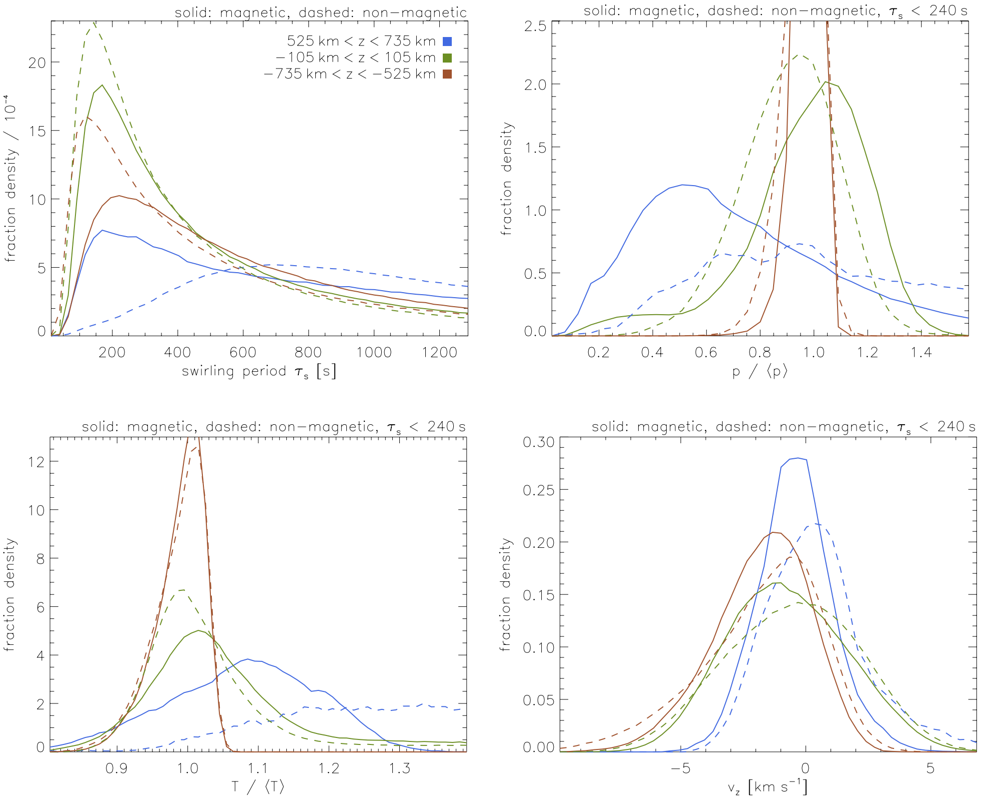

Fig. 5. Histograms of various quantities in swirling regions for three layers of 210 km width each, centered at heights $z = -630$ km, $z = 0$ km, and $z = 630$ km. Solid lines represent the magnetic case, dashed lines the non-magnetic case. The quantities considered are swirling period (*upper left panel*), gas pressure normalized to its horizontal average (*upper right*), temperature normalized to its horizontal average (*lower left*), and vertical velocity component (*lower right*). Each histogram is normalized by its integral.

structure is given in Fig. 8, showing that the post-shock peak temperatures can reach values around 7000 K, which exceed the temperature of the cool background by about 3000 K.

In the magnetic case (Fig. 7), the shock fronts are virtually absent, the divergence of the horizontal velocities typically being an order of magnitude smaller than in the non-magnetic simulation. Apparently, the strong magnetic field suppresses the development of the shock structures. Instead, a small-scale pattern of hot filaments appears in the magnetic regions, which is tightly connected to vertically orientated vortices and localized up- and downflows. The high-temperature features are often associated with the shear part of vorticity.

As an example of the flow structures in the magnetic simulation, Fig. 9 depicts a pair of photospheric vortices in the magnetic case. The velocity streamlines are helically wound with a pitch lower than the height of the photosphere. The magnetic field is expanding with height and not significantly twisted. This is a consequence of the high Alfvén speed in the photosphere, which reaches about 70 km s^{-1} at the upper boundary of the computational box: any twist of the vertical magnetic flux concentrations rapidly escapes upward in the form of torsional Alfvén waves. Such processes may drive swirling flows in the chromosphere (Wedemeyer-Böhm & Rouppe van der Voort 2009) and in the corona (Zhang & Liu 2011).

3.3. Heating processes

Figure 10 shows height profiles of the temporarily and horizontally averaged temperature and dissipation rates (viscous and Ohmic). While the two simulations have very similar temperatures in the deep and near-surface layers, the average atmosphere of the magnetic run shows a much flatter temperature profile above $z \simeq 200$ km. At $z = 600$ km, the temperature difference between the two runs reaches about 600 K. Above this height, the non-magnetic atmosphere shows a steep temperature increase, most likely due to shock heating. The flat profile in the magnetic case indicates a different heating process that extends over a bigger height range and affects also the middle photosphere.

In order to evaluate the importance of viscous and Ohmic dissipation as heating processes, we determined the corresponding specific dissipation rates, i.e., the change of internal energy per unit time and unit mass due to viscous and magnetic diffusion, respectively. The `MURaM` simulations analyzed here were carried out with a physical magnetic diffusion term in the induction equation, assuming a constant magnetic diffusivity of $\eta = 1.1 \times 10^{11}$ cm^2 s^{-1}, the smallest value compatible with the given spatial grid resolution. In contrast, the viscosity term in the momentum equation effectively acts only near the grid scale. It involves artificial diffusivities explicitely depending on the local velocity structure, namely hyperdiffusivities and shock-resolving diffusivities (Vögler et al. 2005). For stability reasons, there is also magnetic hyperdiffusion near the top and bottom of the computational box, but this does not significantly contribute to the dissipation rate below $z \simeq 700$ km.

The bottom panel of Fig. 10 shows the height profiles of the horizontally averaged specific dissipation rates for both runs. The viscous dissipation rate in the non-magnetic case rises steeply above $z \simeq 600$ km, probably related to shock formation in this height range. In the magnetic simulation, the dissipation is dominated by Ohmic dissipation below $z \simeq 500$ km, which exceeds the viscous dissipation by up to a factor of 5 in the middle photosphere. This extended range of heating explains the relatively flat average temperature profile in the magnetic case. The continuous increase of viscous dissipation above $z \simeq 200$ km is

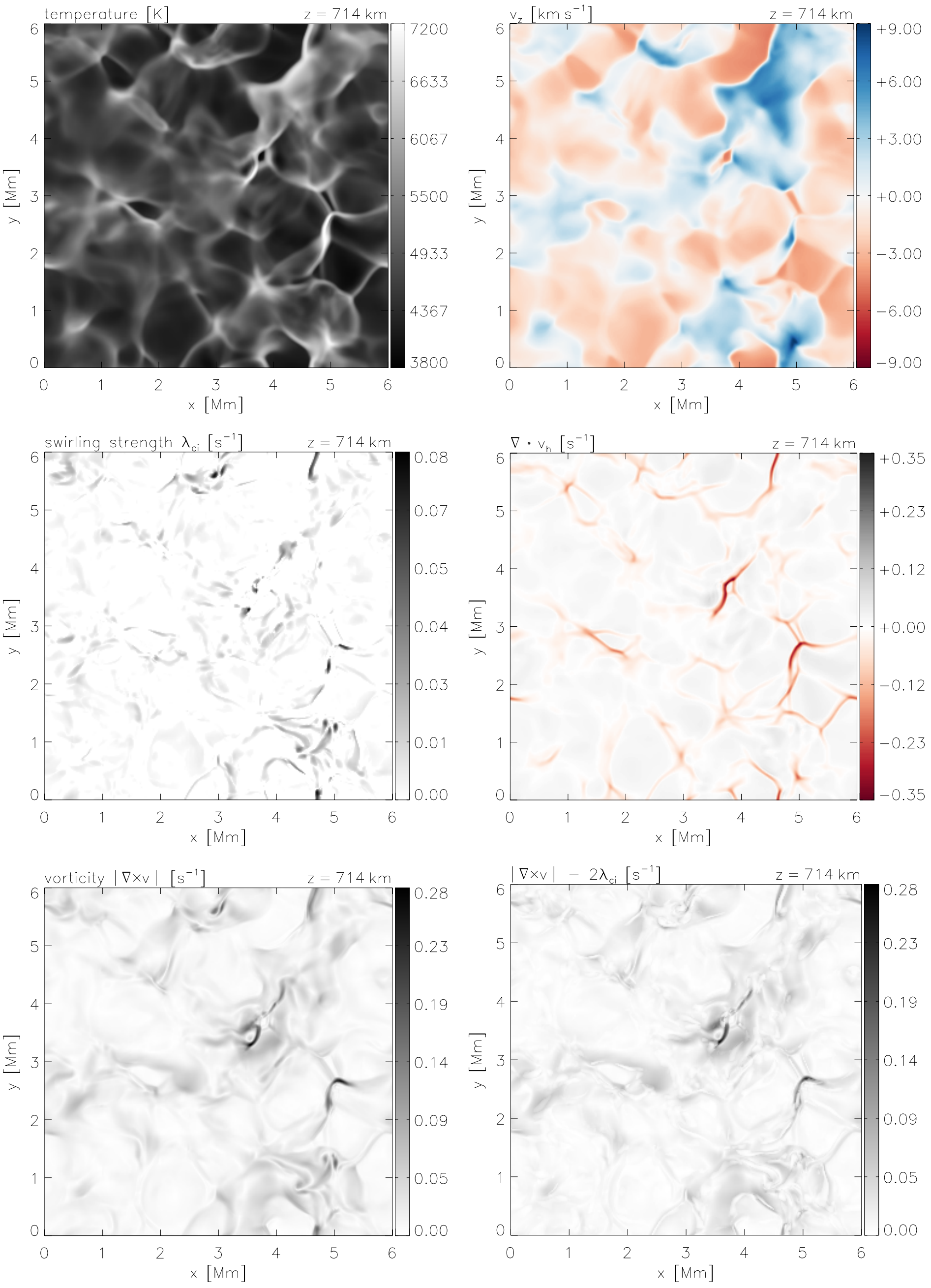

Fig. 6. Horizontal maps of various quantities at $z = 714$ km for the non-magnetic case. *From left to right, top to bottom*: temperature, vertical velocity, swirling strength, divergence of the horizontal velocity, vorticity, and shear part of vorticity.

partly a result of the assumed height profile for the hyperdiffusivity, so that it is possibly overestimated.

Figure 11 provides information about the spatial distribution of the dissipation rates in the higher layers. In the non-magnetic run, the main sources of viscous dissipation are shock fronts. In the magnetic case, the viscous dissipation[2] is associated with the vortices located in the magnetic flux concentrations while the Ohmic dissipation rates are concentrated at the edges of the magnetic flux concentrations.

More detailed and quantitative information on the relation between temperature and flow structure in the upper layers is obtained from the bivariate (2D) histograms shown in Fig. 12. The clearest difference between the non-magnetic case (left column) and the magnetic case (right column) is in the role of the velocity divergence: while there is a strong correlation of negative divergence (associated with shocks) with temperature in the non-magnetic case, such a relation is almost absent in the magnetic run. In both cases, the temperature correlates with swirling strength, but cells with moderate to high swirling strength are much more abundant in the magnetic case. In the non-magnetic simulation, the correlation with swirling strength is due to the association of swirls with shock fronts. Note that the non-magnetic simulation has a much larger proportion of very cool regions with temperatures between 2000 K and 3000 K, which are almost absent in the magnetic case. Both simulations show cells

---

[2] Since the hyperdiffusivities generally are anisotropic, the associated dissipation rates are not necessarily always positive. A few grid cells indeed show slightly negative values of the viscous dissipation rate (see the small isolated white patches in the middle panel of Fig. 11), but these are completely irrelevant for the distribution and the average of the dissipation rates.

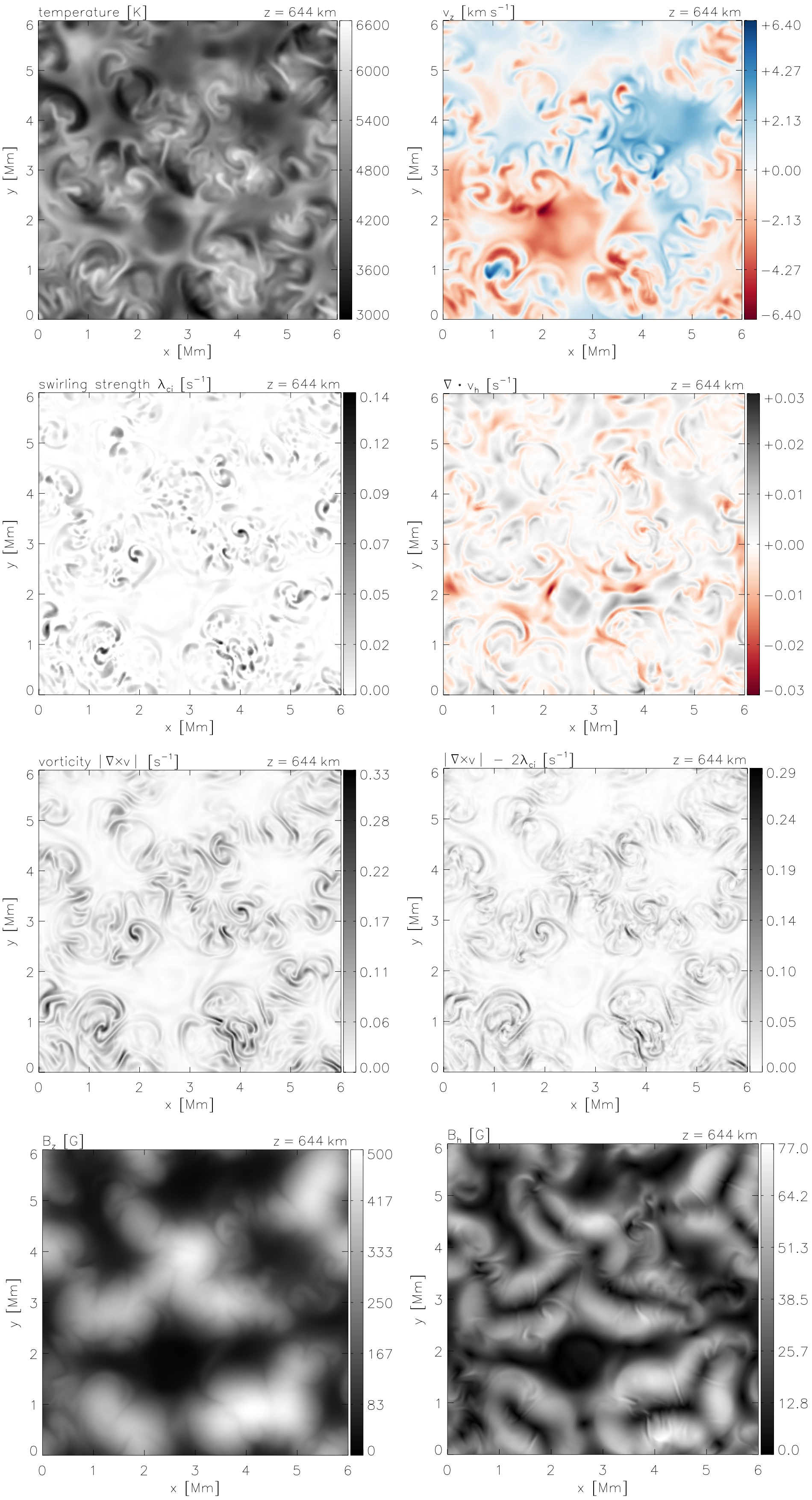

Fig. 7. Horizontal maps of various quantities at z = 644 km for the magnetic case. *From left to right, top to bottom*: temperature, vertical velocity, swirling strength, divergence of the horizontal velocity, vorticity, shear part of vorticity, strength of the vertical magnetic field, and strength of the horizontal magnetic field.

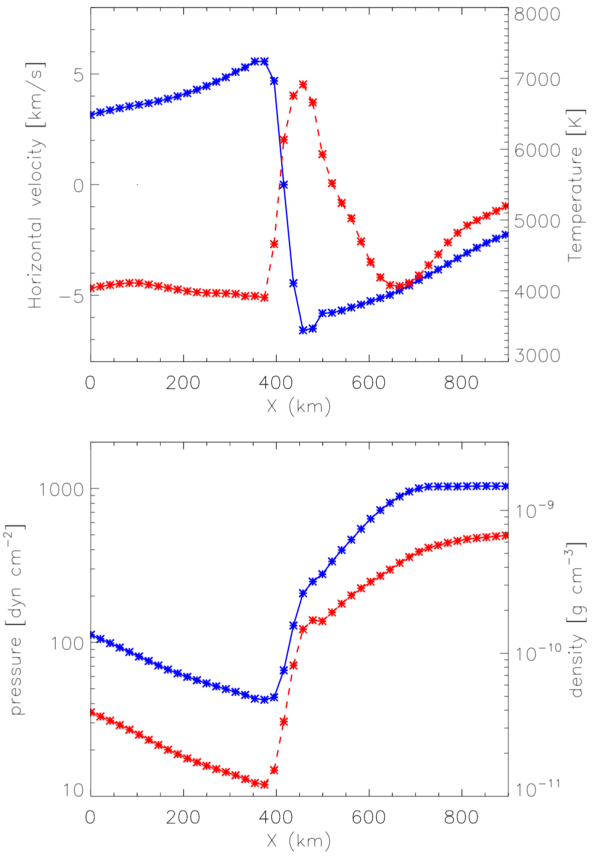

Fig. 8. Horizontal cuts in x-direction through the shock located at $(x, y) = (4.5\,\mathrm{Mm}, 5.7\,\mathrm{Mm})$ in Fig. 6. *Upper panel*: horizontal velocity (blue, solid line) and temperature (red, dashed line); *lower panel*: density (blue, solid line) and gas pressure (red, dashed line).

with high temperature for all values of the swirling strength, but temperatures exceeding 7000 K apparently can only be provided by the shock fronts in the non-magnetic case.

4. Summary and discussion

The simulation results reveal a striking difference between the magnetic and the non-magnetic case in terms of the velocity structure in the upper photosphere and around the temperature-minimum region. While these layers are dominated by shocks in the non-magnetic simulation, the magnetic case is characterized by extended vertical vortices associated with the magnetic flux concentrations. Clearly, there must be a transition from the shock-dominated non-magnetic regime to the vortex-dominated magnetic regime. High-resolution simulations of small-scale dynamo action (Pietarila Graham et al. 2010) indicate that the shock pattern is almost unaffected by the low-lying magnetic loops and occasionally forming vertical flux concentrations generated by the small-scale dynamo. A run simulating the decay of a mixed-polarity field (cf. Cameron et al. 2011) shows that the suppression of the shock pattern sets in for a mean strength of the vertical field component of about 20 G in the lower photosphere. This is consistent with the simulations of Schaffenberger et al. (2006), who find a clear pattern of shock waves for a mean vertical field of 10 G. Consequently, "quiet" regions with a mean unsigned vertical field around 10 G (e.g., Lites et al. 2008) are probably dominated by shock waves, while the upper photosphere of more strongly magnetized unipolar regions (in network and plage) is dynamically dominated by vortices and shear flows associated with the magnetic features.

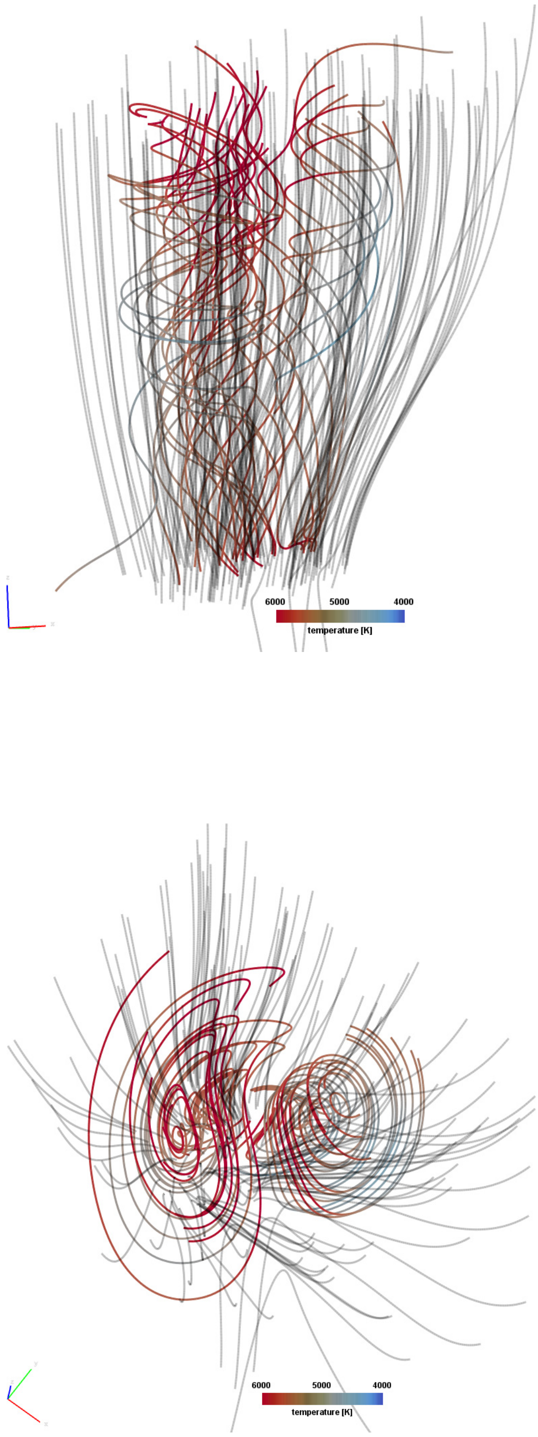

Fig. 9. Streamlines (colored) and magnetic field lines (gray) of two counter-rotating vortices above the optical surface. The vortex pair is located at $(x, y) \simeq (2.0\,\mathrm{Mm}, 2.9\,\mathrm{Mm})$ in Fig. 7. Color represents the temperature.

In both simulations, substantial local heating takes place: shock heating in the top layers of the non-magnetic case and a combination of Ohmic heating (in the lower to middle photosphere) and viscous heating (in the upper photosphere) in the magnetic case. The different height variation of the heating rates in the two cases leads to a sharp temperature rise in the upper layers of the non-magnetic case, in contrast to a more extended

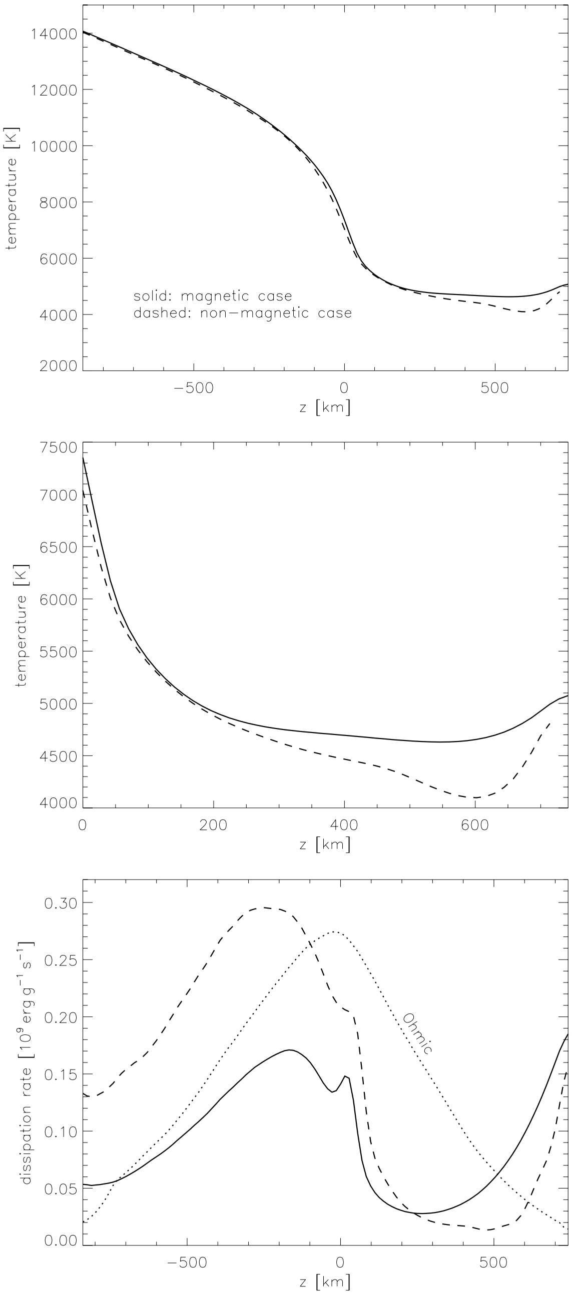

Fig. 10. Height profiles of the horizontally averaged temperature over the full height range (*top panel*) and above the optical surface (*middle panel*). The *bottom panel* shows the horizontally averaged viscous dissipation rates (solid: magnetic case; dashed: non-magnetic case) and the Ohmic dissipation rate in the magnetic case (dotted).

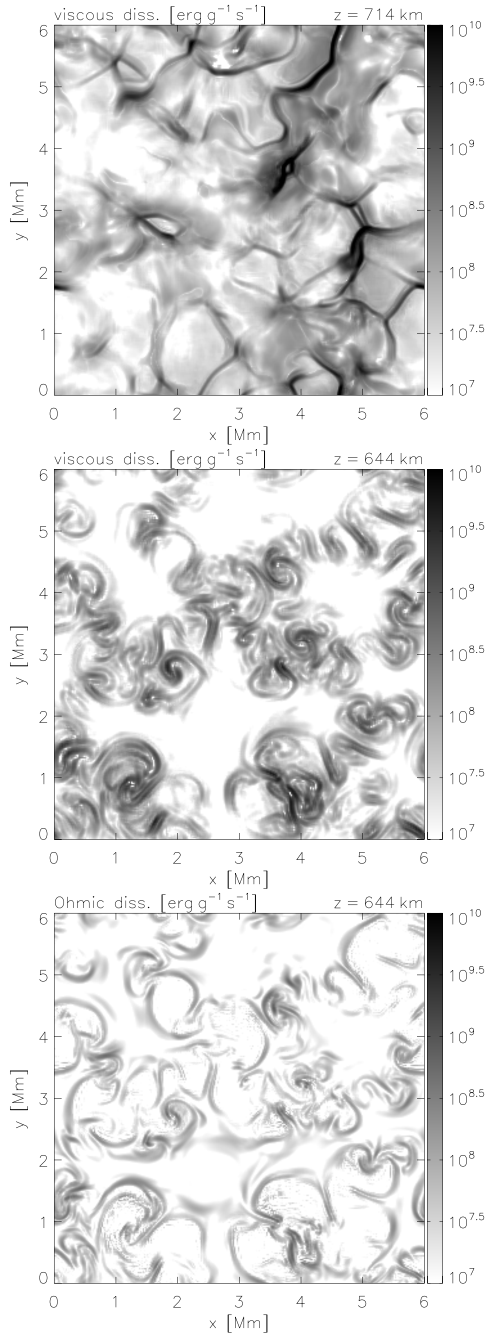

Fig. 11. Dissipation rates on horizontal cuts through the upper photosphere. *Top*: viscous dissipation in the non-magnetic case; *middle*: viscous dissipation in the magnetic case; *bottom*: ohmic dissipation.

temperature enhancement resulting in a flatter temperature gradient in the magnetic run.

However, while yielding important qualitative insight in the different mechanisms for mechanical heating, we do not consider the dissipation rates and thus the temperature structure in the higher layers provided by the simulations to be quantitatively reliable. In the simulation runs considered here, the hyperdiffusive viscous dissipation rate was arbitrarily enhanced in the upper photosphere for reasons of numerical stability, which affects the temperatures. It is also not clear how strongly the dissipation rates depend on the spatial grid resolution and on the assumption of a vertical field at the upper boundary (as opposed to matching to a potential field, for instance). Apart from these problems, we have to keep in mind that the conditions in the layers around the temperature minimum probably deviate from the gray LTE radiative transfer used in the simulations. Furthermore, a direct comparison between horizontal temperature averages (or even averages over surfaces of constant optical depth) from simulations with semi-empirical models would be problematic owing to the strong horizontal inhomogeneities and the nonlinear averaging underlying observed spectral mean line profiles (Uitenbroek & Criscuoli 2011).

We intend to continue this study by carrying out new simulations with an improved treatment of the subgrid scales (see Rempel et al. 2009) and by performing a detailed investigation

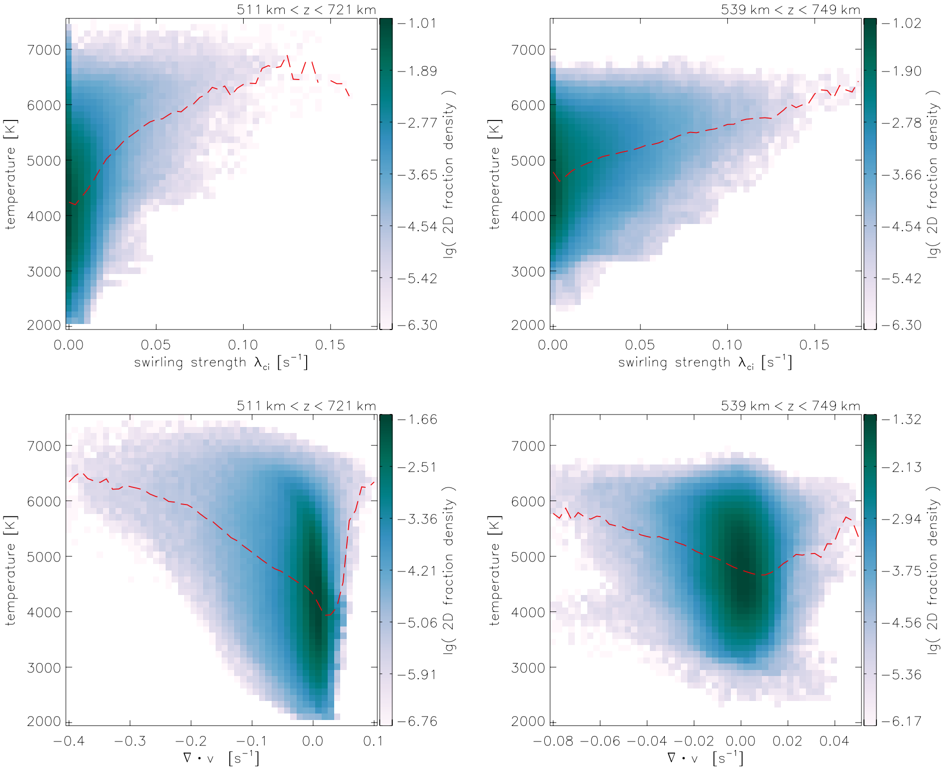

Fig. 12. 2D histograms relating the temperature (vertical axes) to swirling strength (*upper panels*) and velocity divergence (*lower panels*) in the upper photosphere. Results for the non-magnetic case are shown on the *left panels* and those for the magnetic case on the *right panels*. The dashed red lines indicate the mean temperature at a given value of the quantity on the horizontal axis. Each histogram is normalized by its 2D integral.

of the dependence of the dissipation rates on grid resolution and on the upper boundary condition for the magnetic field.

Acknowledgements. This work has been supported by the Max Planck Society in the framework of the Interinstitutional Research Initiative *Turbulent transport and ion heating, reconnection and electron acceleration in solar and fusion plasmas* of the MPI for Solar System Research, Katlenburg-Lindau, and the Institute for Plasma Physics, Garching (project MIF-IF-A-AERO8047).

References

Cameron, R., Vögler, A., & Schüssler, M. 2011, A&A, 533, A86
Carlsson, M., & Stein, R. F. 1992, ApJ, 397, L59
Carlsson, M., & Stein, R. F. 1997, ApJ, 481, 500
Carlsson, M., Hansteen, V. H., & Gudiksen, B. V. 2010, Mem. Soc. Astron. Ital., 81, 582
Curdt, W., Tian, H., & Kamio, S. 2012, Sol. Phys., in press [`arXiv:1201.3199v1`]
Fontenla, J. M., Avrett, E., Thuillier, G., & Harder, J. 2006, ApJ, 639, 441
Kitiashvili, I. N., Kosovichev, A. G., Mansour, N. N., Lele, S. K., & Wray, A. A. 2011, Phys. Scr., submitted [`arXiv:1112.5925v1`]
Kitiashvili, I. N., Kosovichev, A. G., Mansour, N. N., & Wray, A. A. 2012, ApJL, submitted [`arXiv:1201.5442v1`]
Lagg, A., Solanki, S. K., Riethmüller, T. L., et al. 2010, ApJ, 723, L164
Lites, B. W., Kubo, M., Socas Navarro, H., et al. 2008, ApJ, 672, 1237
Moll, R., Cameron, R. H., & Schüssler, M. 2011, A&A, 533, A126
Pietarila Graham, J., Cameron, R., & Schüssler, M. 2010, ApJ, 714, 1606
Rempel, M., Schüssler, M., & Knölker, M. 2009, ApJ, 691, 640
Schaffenberger, W., Wedemeyer-Böhm, S., Steiner, O., & Freytag, B. 2006, in Solar MHD Theory and Observations: A High Spatial Resolution Perspective, ed. J. Leibacher, R. F. Stein, & H. Uitenbroek, ASP Conf. Ser., 354, 345
Shelyag, S., Keys, P., Mathioudakis, M., & Keenan, F. P. 2011, A&A, 526, A5
Solanki, S. K. 1993, Space Sci. Rev., 63, 1
Steiner, O., & Rezaei, R. 2012, in 5th Hinode Science Meeting: Exploring the Active Sun, ed. L. Golub, I. de Moortel, & T. Shimizu, ASP Conf. Ser., in press [`arXiv:1202.4040v1`]
Steiner, O., Franz, M., Bello González, N., et al. 2010, ApJ, 723, L180
Uitenbroek, H., & Criscuoli, S. 2011, ApJ, 736, 69
Vögler, A. 2003, Ph.D. Thesis, University of Göttingen, Germany, `http://webdoc.sub.gwdg.de/diss/2004/voegler`
Vögler, A. 2004, in The Sun and Planetary Systems – Paradigms for the Universe, ed. E. Schielicke (Weinheim, Germany: Wiley-VCH), Rev. Mod. Astron., 17, 69
Vögler, A., Shelyag, S., Schüssler, M., et al. 2005, A&A, 429, 335
Wedemeyer-Böhm, S. 2010, Mem. Soc. Astron. Ital., 81, 693
Wedemeyer-Böhm, S., & Rouppe van der Voort, L. 2009, A&A, 507, L9
Wedemeyer, S., Freytag, B., Steffen, M., Ludwig, H.-G., & Holweger, H. 2004, A&A, 414, 1121
Zhang, J., & Liu, Y. 2011, ApJ, 741, L7
Zhou, J., Adrian, R. J., Balachandar, S., & Kendall, T. M. 1999, J. Fluid Mech., 387, 353